



# Importance of microphysical settings for climate forcing by stratospheric SO<sub>2</sub> injections as modelled by SOCOL-AERv2

Sandro Vattioni<sup>1,\*</sup>, Andrea Stenke<sup>1,2,3,\*</sup>, Beiping Luo<sup>1</sup>, Gabriel Chiodo<sup>1</sup>, Timofei Sukhodolov<sup>4</sup>, Elia Wunderlin<sup>1</sup>, and Thomas Peter<sup>1</sup>

<sup>1</sup>Institute for Atmospheric and Climate Science, ETH Zurich, Switzerland

<sup>2</sup>Institute of Biogeochemistry and Pollutant Dynamics, ETH Zurich, Switzerland

<sup>3</sup>Eawag, Swiss Federal Institute of Aquatic Science and Technology, Dübendorf, Switzerland

<sup>4</sup>Physikalisch-Meteorologisches Observatorium Davos and World Radiation Center, Davos, Switzerland

\*These authors contributed equally to this work.

**Correspondence:** Sandro Vattioni (sandro.vattioni@env.ethz.ch), Andrea Stenke (andrea.stenke@env.ethz.ch)

**Abstract.** Solar radiation management as a sustained deliberate source of SO<sub>2</sub> into the stratosphere (strat-SRM) has been proposed as an option for climate intervention. Global interactive aerosol-chemistry-climate models are often used to investigate the potential cooling efficiencies and side effects of hypothesised strat-SRM scenarios. A recent strat-SRM model intercomparison study for composition-climate models with interactive stratospheric aerosol suggests that the modelled climate response to a particular assumed injection strategy, depends on the type of aerosol microphysical scheme used (e.g., modal or sectional representation), alongside also host model resolution and transport. Compared to short-duration volcanic SO<sub>2</sub> emission, the continuous SO<sub>2</sub> injections in strat-SRM scenarios may pose a greater challenge to the numerical implementation of microphysical processes such as nucleation, condensation, and coagulation. This study explores how changing the timesteps and sequencing of microphysical processes in the sectional aerosol-chemistry-climate model SOCOL-AERv2 (40 size bins) affect model predicted climate and ozone layer impacts considering strat-SRM SO<sub>2</sub> injections of 5 and 25 Tg(S) yr<sup>-1</sup> at 20 km altitude between 30°S and 30°N. The model experiments consider year 2040 boundary conditions for ozone depleting substances and green house gases. We focus on the length of the microphysical timestep and the call sequence of nucleation and condensation, the two competing sink processes for gaseous H<sub>2</sub>SO<sub>4</sub>. Under stratospheric background conditions, we find no effect of the microphysical setup on the simulated aerosol properties. However, at the high sulfur loadings reached in the scenarios injecting 25 Mt/yr of sulfur with a default microphysical timesetp of 6 min, changing the call sequence from the default "condensation first" to "nucleation first" leads to a massive increase in the number densities of particles in the nucleation mode ( $R < 0.01 \mu\text{m}$ ) and a small decrease in coarse mode particles ( $R > 1 \mu\text{m}$ ). As expected, the influence of the call sequence becomes negligible when the microphysical timestep is reduced to a few seconds, with the model solutions converging to a size distribution with a pronounced nucleation mode. While the main features and spatial patterns of climate forcing by SO<sub>2</sub> injections are not strongly affected by the microphysical configuration, the absolute numbers vary considerably. For the extreme injection with 25 Tg(S) yr<sup>-1</sup>, the simulated net global radiative forcing ranges from  $-2.3 \text{ W m}^{-2}$  to  $-5.3 \text{ W m}^{-2}$ , depending on the microphysical configuration. "Nucleation first" shifts the size distribution towards radii better suited for solar scattering ( $0.3 \mu\text{m} < R < 0.4 \mu\text{m}$ ), enhancing the intervention efficiency. The size-distribution shift however generates more

ultra-fine aerosol particles, increasing the surface area density, resulting in 10 DU less ozone (about 3% of total column) in  
25 the northern midlatitudes and 20 DU less ozone (6%) over the polar caps, compared to the "condensation first" approach. Our  
results suggest that a reasonably short microphysical time step of 2 minutes or less must be applied to accurately capture the  
magnitude of the  $\text{H}_2\text{SO}_2$  supersaturation resulting from  $\text{SO}_2$  injection scenarios or volcanic eruptions. Taken together these  
results underscore how structural aspects of model representation of aerosol microphysical processes become important under  
conditions of elevated stratospheric sulfur in determining atmospheric chemistry and climate impacts.

## 30 1 Introduction

The idea of increasing the Earth's albedo by injecting sulfur containing gases into the stratosphere to reduce some of the  
adverse effects of greenhouse-gas (GHG) induced global warming dates back to the 1970s (Budyko, 1974), and was 30 years  
later further elaborated by Crutzen (2006). The arguments presented by Crutzen called for active scientific research of the  
kind of activity, which became known under the somewhat misleading term "geoengineering". We term this here "climate  
35 intervention", following the recommendation of the National Research Council (2015). Crutzen's idea is based on the fact that  
sulfur containing gases, such as  $\text{SO}_2$ ,  $\text{H}_2\text{S}$  or  $\text{OCS}$ , injected into the lower stratosphere will form aqueous sulfuric acid aerosol  
particles via a chain of chemical and microphysical processes (Thomason and Peter, 2006; Kremser et al., 2016). The resulting  
binary  $\text{H}_2\text{SO}_4$ - $\text{H}_2\text{O}$  solution droplets reflect solar radiation back to space, causing a cooling at the Earth's surface. At the same  
time, however, they heat the stratosphere due to absorption of upwelling long-wave radiation. Moreover, sulfate aerosols play  
40 an important role in stratospheric ozone chemistry by providing surfaces for heterogeneous reactions (Solomon, 1999). While  
the infrared absorptivity is determined to good approximation by the total aerosol volume, the efficiency of scattering solar  
radiation depends strongly on the detailed aerosol size distribution: Many small particles are more efficient than a few large  
particles, but they also provide a larger surface area density (SAD) accelerating heterogeneous chemistry (Heckendorn et al.,  
2009).

45 In the stratosphere, the total aerosol number density and size distribution are governed by the microphysical processes of  
nucleation, coagulation, condensation, evaporation, and gravitational settling (Kremser et al., 2016, and references therein).  
The formation of new sulfate aerosol particles occurs via binary homogeneous nucleation of  $\text{H}_2\text{SO}_4$  and  $\text{H}_2\text{O}$  molecules, or,  
via heterogeneous nucleation in the presence of appropriate condensation nuclei like meteoritic dust or ions, which requires  
lower saturation ratios than homogeneous nucleation. The freshly formed particles can grow further through coagulation as  
50 well as condensation of  $\text{H}_2\text{SO}_4$  (together with  $\text{H}_2\text{O}$ ). As stratospheric temperatures increase with altitude, the sulfate aerosol  
particles eventually evaporate above 32 to 35 km, releasing  $\text{H}_2\text{SO}_4$  back to the gas phase.

The effectiveness of climate intervention by  $\text{SO}_2$  emission has been intensively investigated by using models of different  
complexity and assuming different injection scenarios (e.g., Heckendorn et al., 2009; Pierce et al., 2010; Niemeier et al.,  
2011; English et al., 2011; Niemeier and Timmreck, 2015; Tilmes et al., 2018; Vattioni et al., 2019; Weisenstein et al., 2022;  
55 Laakso et al., 2022; Visoni et al., 2022). Such modelling studies have advanced our understanding of stratospheric aerosols,  
but they also highlighted uncertainties regarding the transport, chemistry, and microphysics of the aerosol size distribution.



In a recent study, Weisenstein et al. (2022) presented a model intercomparison exploring the impacts of stratospheric injections of  $\text{SO}_2$  gas as well as accumulation-mode sulfuric acid aerosol ( $\text{AM-H}_2\text{SO}_4$ ) on atmospheric chemistry and climate. Three general circulation models (GCMs) with interactive aerosol microphysics conducted strictly coordinated model experiments within the framework of the Geoengineering Model Intercomparison Project (GeoMIP, Kravitz et al., 2011), namely the Community Earth System Model (CESM2) with the Whole Atmosphere Community Climate Model (WACCM) atmospheric configuration (Danabasoglu et al., 2020), the middle atmosphere version of ECHAM5 with the HAM microphysical module (MAECHAM5-HAM; Stier et al., 2005), and the SOLar Climate Ozone Links model with AER microphysics (SOCOL-AER) version 2 (Feinberg et al., 2019). The model experiments included injections of 5 and 25  $\text{Tg(S) yr}^{-1}$  in form of  $\text{SO}_2$  gas or  $\text{AM-H}_2\text{SO}_4$ , emitted either as two point injections at  $30^\circ\text{N}$  and  $30^\circ\text{S}$  or as regional injection between  $30^\circ\text{N}$  and  $30^\circ\text{S}$ . Two of the participating models, CESM2 and MAECHAM5-HAM, assume the aerosol size distribution can be described by superimposed lognormal size distributions (modal scheme), while Socol-AERv2 uses a size bin-resolving (sectional) scheme.

The analysis of the simulated particle size distributions for the  $\text{SO}_2$  injection scenarios revealed substantial differences between each pair of the three models. CESM2 generates new particles and adds them directly to the Aitken mode ( $R \gtrsim 10$  nm), so that there are no nm-sized particles. In contrast, Socol-AERv2 treats these tiny particles down to 0.4 nm. Compared to MA-EACHM-HAM, Socol shows substantially fewer nucleation mode particles, suggesting different roles of nucleation and condensation in both models: the microphysical scheme in Socol-AERv2 appears to prefer condensational growth of existing particles by uptake of  $\text{H}_2\text{SO}_4$  over the formation of new particles, while the opposite seems to be the case for MAECHAM5-HAM. The description of the results of the microphysical processes by means of lognormal functions in modal models, such as CESM2 and MAECHAM5-HAM, further complicates the interpretation.

Nucleation and condensation are competing sink processes for gas-phase  $\text{H}_2\text{SO}_4$ , which occur simultaneously in the atmosphere, but typically with different speeds. The characteristic time scale  $\tau$  for removal of  $\text{H}_2\text{SO}_4$  molecules by condensation is given by the following equation:

$$\tau_{\text{cond}} = \frac{4}{Av}, \quad (1)$$

with  $A$  being the aerosol surface area density and  $v$  the mean thermal velocity of  $\text{H}_2\text{SO}_4$  molecules. For background conditions with typical SAD values of 5 to  $10 \mu\text{m}^2\text{cm}^{-3}$  in nucleation regions, the equilibrium time scale for condensation is around 0.5–1 h. This value decreases inversely with increasing SAD. Under volcanic or geoengineered conditions with  $\text{SAD} \sim 80 \mu\text{m}^2\text{cm}^{-3}$ , typical for the 25  $\text{Tg(S) yr}^{-1}$  injection scenario, the equilibrium time scale is less than 5 minutes. As the nucleation rate strongly depends on the gas-phase  $\text{H}_2\text{SO}_4$  supersaturation, the model timestep used for condensation and nucleation must be significantly smaller than the time required to approach gas-phase equilibrium in order to avoid that one process erroneously dominates the gas-to-particle transfer of  $\text{H}_2\text{SO}_4$ . Furthermore, coagulation is also affected by the competition between nucleation and condensation, as it is most efficient at (initially) high number densities and between particles of different size. Small particles move fast, but have only small cross-sections for collision, while large particles have a slower Brownian motion, but provide good collision targets for smaller particles (Seinfeld and Pandis, 1997). The correct numerical representation of these simultaneously occurring processes is challenging, especially under sulfur-rich conditions, when characteristic time



scales become extremely short. This motivated us to critically question the microphysical scheme of the sectional SOCOL-AERv2 model and to systematically test the impact of the call sequence of the subroutines for condensation and nucleation, as well as the microphysical timestep on the simulated aerosol properties and the modeled climate response to stratospheric SO<sub>2</sub> injection.

95 The paper is organised as follows: Section 2 presents a brief description of the SOCOL-AERv2 model and details of the experimental setup. Section 3 discusses the impact the microphysical settings on the aerosol size distribution under stratospheric background conditions as well as under stratospheric injections of SO<sub>2</sub> gas (3.1), on the global mean particle size, aerosol burden and radiative forcing (3.2), and on the meridional distributions of aerosol burden, radiative forcing, and ozone (3.3) resulting from the SO<sub>2</sub> injections. The influence of the microphysical settings on profiles of various quantities is briefly  
100 mentioned (3.4) and detailed in the Supplement. To evaluate the changes in SOCOL aerosol microphysics against observations we also tested different settings for the 1991 eruption of Mt. Pinatubo (3.5). Section 4 includes a summary and discussion.

## 2 Model description and experimental setup

### 2.1 SOCOL-AERv2

A first version of the aerosol-chemistry-climate model SOCOL-AER had been introduced by Sheng et al. (2015), who integrated the size-resolving (sectional) sulfate aerosol module AER (Weisenstein et al., 1997) into the three dimensional grid of the chemistry-climate model (CCM) SOCOLv3 (Stenke et al., 2013), which consists of the middle atmosphere version of the spectral general circulation model MA-ECHAM5 (Roeckner et al., 2003, 2006) and the chemistry-transport model MEZON (Rozanov et al., 1999; Egorova et al., 2003). Since then, the model's tropospheric and stratospheric sulfur cycle have undergone several improvements, resulting in the publication of SOCOL-AERv2 (Feinberg et al., 2019).  
105

110 SOCOL-AERv2 resolves the sulfate aerosol particles in 40 size bins, ranging from 0.39 nm to 3.2 μm in radius. Since the size bins refer to dry aerosol radius, they can also be interpreted as aerosol H<sub>2</sub>SO<sub>4</sub> mass bins, ranging from about 2.8 molecules to  $1.6 \times 10^{12}$  molecules of H<sub>2</sub>SO<sub>4</sub> per aerosol particle. Neighboring size bins differ by molecule number doubling.

Detailed descriptions of the original AER microphysics and their adaptations for the coupled model are provided in Weisenstein et al. (1997, 2007) and Sheng et al. (2015), respectively. Aerosol composition, i.e. the sulfuric acid weight percent in the particles, is calculated as function of ambient temperature and H<sub>2</sub>O partial pressure using the parameterization of Tabazadeh et al. (1997), which is also used for the calculation of the wet aerosol radius of each size bin. For the formation of new particles by binary homogeneous nucleation the scheme of Vehkamäki et al. (2002) is used. The scheme calculates the nucleation rate as well as the radius and composition of new particles, meaning that the nucleated mass is added to a single size bin. The particles can grow through H<sub>2</sub>SO<sub>4</sub> condensation and shrink through evaporation, both processes depending on the equilibrium  
115 concentration of H<sub>2</sub>SO<sub>4</sub> above the particle surface (Ayers et al., 1980; Kulmala and Laaksonen, 1990). Condensational growth leads to an increase of mass in the aerosol phase and a shift of particles to larger size bins, while evaporation does the opposite. Changes in the net number density occur only upon evaporation from the smallest size bin or condensational growth of the  
120 largest size bin. Finally, coagulation reduces number densities and shifts aerosol mass to larger bins. Coagulation is solved by a



semi-implicit method (Jacobson and Seinfeld, 2004), whereas at most 90% of the available mass in one size bin is allowed to be  
125 lost by coagulation within one microphysical time step. Otherwise, the coagulation timestep is reduced. The coagulation kernel, which defines the collision probability of two particles, depends on the particle radius and the diffusion coefficient (Fuchs, 1964). Finally, sedimentation, which affects the vertical distribution of aerosol particles and reduces their residence time in the stratosphere, is parameterised following the numerical scheme of Walcek (2000). The gravitational settling velocities of aerosol particles are calculated following Kasten (1968).

130 The CCM SOCOLv3 and the aerosol module AER are interactively coupled via the chemistry and radiation routines. Sulfur chemical reactions (Sheng et al., 2015, see Table 1) are fully integrated into the model's chemical solver, which is based on the implicit iterative Newton-Raphson scheme (Stott and Harwood, 1993). In addition to gas-phase chemistry, the model includes aqueous-phase oxidation of S(IV) to S(VI) by ozone ( $O_3$ ) and hydrogen peroxide ( $H_2O_2$ ) in cloud water (Jacob, 1986). The modeled sulfate aerosol is fed directly into the heterogeneous chemistry and radiation schemes. The aerosol radiative  
135 properties (extinction coefficients, single scattering albedos, and asymmetry factors as functions of wavelength) required to drive the model dynamics are calculated online from the aerosol size distribution using Mie theory with a temperature- and humidity-dependent look-up table, which accounts for the aerosol  $H_2O_2$  weight percent.

The model uses operator splitting. The dynamics module is called every 15 min, whereas the chemistry, aerosol micro-  
physics, and radiation schemes are called every 2 h. For the microphysical processes, especially for nucleation with its highly  
140 nonlinear dependence on gaseous  $H_2SO_4$  concentration, sub-timesteps are used within the 2-h chemistry loop, to avoid that the process called first mistakenly dominates the  $H_2SO_4$ -to-particle exchange rate. The default procedure is to use  $N_{\text{micro}} = 20$  sub-loops within the chemical timestep, which results in a microphysical timestep of 6 minutes ( $2 \text{ h}/N_{\text{micro}} = 2 \text{ h}/20 = 6 \text{ min}$ ). The parameter  $N_{\text{micro}}$  can be easily adjusted between runs. By default, the call sequence for the microphysical processes is condensation first, followed by nucleation (see "CN" sequence in Fig. 1), and finally coagulation. At each chemical timestep,  
145 the model first calculates the new  $H_2SO_4$  gas-phase concentration resulting from chemical production and transport. In the microphysical loop, the  $H_2SO_4$  concentration is then consecutively updated by condensation and nucleation. As we will see later, it is also important to distribute the gaseous  $H_2SO_4$  molecules produced during the 2-h chemical timestep homogeneously over the  $N_{\text{micro}}$  sub-timesteps (see  $\Delta H_2SO_4$  in Fig. 1), rather than passing them as a total amount at the beginning of the microphysical loop. Otherwise, under conditions of  $SO_2$  injections the 2-hourly call frequency of the chemistry scheme would lead  
150 to initially unrealistically high  $H_2SO_4$  supersaturations in the microphysical loop, which then causes artefacts in the aerosol microphysics. The aerosol composition as well as the coagulation kernel are calculated only once every 2 h and are kept constant for the microphysical calculations. Finally, sedimentation is calculated after the microphysical subloop, again once every 2 h. To test the implications of the aerosol microphysics on the simulated aerosol size distribution under various stratospheric sulfur loadings, we performed several sensitivity simulations, for which we changed the call sequence for condensation and  
155 nucleation or increased the number of microphysical sub-timesteps  $N_{\text{micro}} > 20$ .

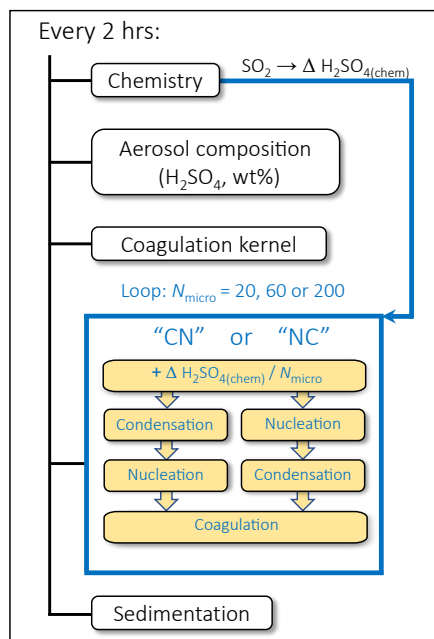


**Figure 1.** Schematic representation of the call sequence for the microphysical processes in SOCOL-AERv2. The scheme shows the setup with the microphysical subloop with  $N_{\text{micro}} = 20$  steps by default, or an increased number of steps (60, 80, or 200) in the test runs. By default, the condensation routine is called first and nucleation second ("CN"), which was reversed ("NC") for the tests. Furthermore, the amount of  $\text{H}_2\text{SO}_2$  gas molecules produced by the chemistry scheme is uniformly distributed over the  $N_{\text{micro}}$  time steps, instead of providing the total amount at the first microphysical time step, as done in the original set-up.

## 2.2 SOCOLv4

160 Additionally, we performed simulations with the fully coupled Earth System Model (ESM) SOCOLv4 (Sukhodolov et al., 2021), which is a further development of SOCOL-AERv2. SOCOLv4, incorporates the same aerosol module, AER, as SOCOL-AERv2 (Sect. 2.1). The major differences between the model versions is that SOCOLv4 is based on the MPI-ESM1.2 (Mau-  
165 ritsen et al., 2019), which incorporates the fully coupled interactive ocean module MPIOM (Jungclaus et al., 2013). SOCOLv4 has a finer horizontal and vertical resolution with T63 truncation ( $1.9^\circ \times 1.9^\circ$ ) and 47 vertical pressure levels also reaching up to 0.01 hPa. Compared to SOCOL-AERv2 the default dynamical timestep was halved to 7.5 min, while the default chemical and microphysical time steps are the same as for SOCOL-AERv2 (2h and 6 min, respectively). The interactive ocean as well as the finer spatial resolution make SOCOLv4 computationally much more expensive than SOCOL-AERv2. Therefore, we  
165 performed most sensitivity simulations with SOCOL-AERv2 using fixed sea surface temperatures (SST) and sea ice coverage (SIC, see section 2.3), while SOCOLv4 was primarily used to look at the impact on surface temperature anomalies.





## 2.3 Experimental setup

For the present study, we employed SOCOL-AERv2 with a resolution of 39 hybrid sigma-pressure levels in the vertical and a horizontal truncation of T42 ( $\sim 2.8^\circ \times 2.8^\circ$  in latitude and longitude). The simulations for this study include a reference scenario for stratospheric background conditions as well as two perturbation scenarios including stratospheric sulfur injections. The boundary conditions are identical to the GeoMIP test-bed experiment "accumH2SO4"<sup>1</sup> with GHGs and ozone-depleting substances taken from the projections for 2040 from the SSP5-8.5 scenario (see also Weisenstein et al. (2022)). SST and SIC are prescribed using an average of the years 1988–2007 of the CMIP5 PCMDI-AMIP-1.1.0 SST/Sea Ice dataset (Taylor et al., 2000). As SOCOL-AERv2 with 39 vertical levels does not generate a quasi-biennial oscillation (QBO) internally, the simulated wind in the equatorial stratosphere is nudged towards observed wind profiles (Stenke et al., 2013). We ran 20 model years for each scenario. The first 5 years are considered as spin-up period (sufficient for the present application), and we use the subsequent 15 years for our analysis.

Consistent with Weisenstein et al. (2022), the intervention scenarios examined here apply gaseous SO<sub>2</sub> injections of 5 and 25 Tg(S) yr<sup>-1</sup> emitted uniformly in a 2 km thick layer centred around 20 km altitude in the region between 30°S and 30°N over all longitudes. These so-called "regional injections" are complemented by an example of a "point injection" performed with SOCOLv4 (see section 2.2) injecting 5 Tg(S) yr<sup>-1</sup> of SO<sub>2</sub> at the same vertical extent but constrained to a region from 10°N to 10°S at the equator only emitting at the 0° meridian. These point emission scenarios followed the G4 GeoMIP scenario (Kravitz et al., 2011) with transient SSP5-8.5 boundary conditions and allow us to explore the sensitivity of surface temperature to the call sequence in a fully coupled ESM.

To determine the effects of the setup of the microphysical scheme (see Fig. 1) on the computed size distribution and aerosol burden, we performed several model simulations for background conditions as well as conditions of climate intervention. The different simulations vary by reversing the call sequence of the condensation and nucleation routines, or by increasing the number of microphysical timesteps  $N_{\text{micro}}$ . The model simulations are summarized in Table 1. The experiment BG\_CN\_20 represents the default setup of the microphysical scheme in SOCOL-AERv2 and is used as the reference simulation.

In the absence of observational data of the stratospheric aerosol layer under geoengineering conditions, we also tested the effect of different microphysical settings in the modeling of the 1991 Mt. Pinatubo eruption, following the experimental setup of the Interactive Stratospheric Aerosol Model Intercomparison Project (ISA-MIP, Quaglia et al., 2023).

## 3 Results

In this section, we first analyze how the microphysical settings in SOCOL-AERv2 affect the calculated aerosol size distributions under stratospheric background conditions and under scenarios with SO<sub>2</sub> injection. Next, we examine how the changes in size distributions affect global aerosol properties, such as aerosol loading and net radiative forcing. Finally, we show that

<sup>1</sup>Details of the experiment protocol: <http://climate.envsci.rutgers.edu/geomip/testbed.html>



**Table 1.** Overview of model simulations performed with SOCOL-AERv2 (except for S5p, which was performed with SOCOLv4). Simulation names refer to the following naming convention: "SO<sub>2</sub> emission scenario"\_"Call sequence"\_" $N_{\text{micro}}$ ". BG: background; S5: 5 Tg(S)yr<sup>-1</sup>, regional emission; S5p: 5 Tg(S)yr<sup>-1</sup>, point emission simulated with SOCOLv4; S25: 25 Tg(S)yr<sup>-1</sup>, regional emission; PIN: Pinatubo eruption ("shallow injection" scenario of ISA-MIP (Timmreck et al., 2018)); CN: condensation first; NC: nucleation first;  $N_{\text{micro}}$ : number of microphysical timesteps.

Simulation name	SO <sub>2</sub> emission scenario	Microphysical call sequence	Microphysical timesteps
BG_CN_20	background	Cond-Nuc	20
BG_NC_20		Nuc-Cond	20
S5_CN_20	5 Tg(S) yr <sup>-1</sup> (regional)	Cond-Nuc	20
S5_CN_200		Cond-Nuc	200
S5_NC_20		Nuc-Cond	20
S5_NC_200		Nuc-Cond	200
S5p_CN_20	5 Tg(S) yr <sup>-1</sup> (point)	Cond-Nuc	20
S5p_NC_20		Nuc-Cond	20
S25_CN_20	25 Tg(S) yr <sup>-1</sup> (regional)	Cond-Nuc	20
S25_CN_200		Cond-Nuc	200
S25_NC_20		Nuc-Cond	20
S25_NC_60		Nuc-Cond	60
S25_NC_200		Nuc-Cond	200
PIN_CN_20	Pinatubo 5 Tg(S) (single event, point)	Cond-Nuc	20
PIN_NC_20		Nuc-Cond	20
PIN_NC_200		Nuc-Cond	200

microphysical settings directly affect stratospheric chemistry and thus the ozone layer via aerosol surface area density under conditions with climate intervention.

### 3.1 Influence of microphysical settings on aerosol size distribution

200 The upper row of panels in Fig. 2 shows particle size distributions at 55 hPa in the low latitudes (30°S-30°N) for unperturbed and for conditions with climate intervention. As obvious from panel (a), changing the call sequence of the nucleation and condensation subroutines does not influence the simulated aerosol size distribution under background conditions. Since maximum nucleation rates occur about 2-3 km below the tropical tropopause (Thomason and Peter, 2006), we also examined the size distributions at 115 hPa (not shown), and again find that the call sequence has no impact on the model results. This indicates that





205 the default microphysical timestep of 6 min is sufficiently shorter than the characteristic times of nucleation and condensation under background conditions, so that none of the two processes inappropriately dominates the  $\text{H}_2\text{SO}_4$ -to-particle conversion.

In contrast to background conditions, the  $\text{SO}_2$  injections scenarios are highly sensitive to the microphysical settings. Initially, we kept the microphysical timestep constant ( $N_{\text{micro}} = 20$ ), but reversed the call sequence from the default "condensation first" (CN) to "nucleation first" (NC). This modification leads to a massive increase of nucleation mode particles ( $R < 0.01 \mu\text{m}$ )  
210 (Fig. 2c, e, yellow and blue dotted lines).

To highlight differences in the coarse mode ( $R > 1 \mu\text{m}$ ), we calculated the fifth moment of the corresponding size distributions (lower row in Fig. 2). This provides an estimate of the downward mass flux due to aerosol sedimentation, which is determined by the product of particle volume (proportional to the third moment) and sedimentation speed (roughly proportional to the second moment). Swapping from CN to NC leads to a significant decrease of coarse mode particles (by one order  
215 of magnitude) for the S25 scenario (inset in Fig. 2f).

These significant differences in the size distributions demonstrate the dominating role of the first-called process as  $\text{H}_2\text{SO}_4$  sink, either condensation or nucleation, indicating that the default timestep ( $2 \text{ h}/N_{\text{micro}} = 2 \text{ h}/20 = 6 \text{ min}$ ) is too long to properly handle elevated stratospheric sulfur loadings. Therefore, we increased the number of microphysical substeps until the resulting particle size distributions of the CN and CN simulations converge. For a sufficiently short microphysical timestep (0.6 min  
220 with  $N_{\text{micro}} = 200$ ), the simulations develop a pronounced peak of nucleation mode particles (Fig. 2c, e, orange and blue solid lines) similar to the CN\_20 simulations, but with somewhat lower particle number densities.

As expected, the computational costs of the model increase with a shorter microphysical timestep. Increasing the number of microphysical substeps from 20 to 200 almost doubles the required wall-clock time per model year from 4.6 h to 9 h, using parallel computing on 64 CPUs. To assess possibilities to reduce the computational costs, we tested the efficiency of  
225  $N_{\text{micro}} = 60$  (and 80, not shown).

The red lines in Fig. 2e,f show the results for S25\_CN\_60, demonstrating excellent agreement with  $N_{\text{micro}} = 200$ , which gives us confidence in the accuracy of the model solution. Furthermore, the computational demand increased only moderately by about 33% (60 min) per model year (relative to  $N_{\text{micro}} = 20$ ). In conclusion, in SOCOL-AERv2 nucleation first with  
230  $N_{\text{micro}} = 60$  provides a very good description of climate intervention scenarios, even when the loading is extremely high.

We also explored the effects of the distribution of gaseous  $\text{H}_2\text{SO}_4$  molecules produced during the 2-hourly call of the chemistry routine, either homogeneously across the  $N_{\text{micro}}$  sub-timesteps or as a total amount at the beginning of the microphysical loop. As Fig. S1 in the Supplement shows, proper partitioning of the  $\text{H}_2\text{SO}_4$  molecules among the  $N_{\text{micro}}$  sub-timesteps is critical to avoid an excessive formation of nucleation mode particles due to artificially high  $\text{H}_2\text{SO}_4$  supersaturations at the beginning of the microphysical substepping. More details can be found in the supplementary material (see Section S2).

### 235 3.2 Influence of microphysical settings on global means of particle size, aerosol burden and radiative forcing

The large differences in the simulated size distribution have wide implications for other key metrics of stratospheric aerosols, namely the average size of the aerosol particles, burden and radiative forcing: these are collectively shown in Fig. 3 in the three sets of experiments. Figure 3a shows the globally averaged effective radius ( $R_{\text{eff}}$ ) at 55 hPa. For background conditions

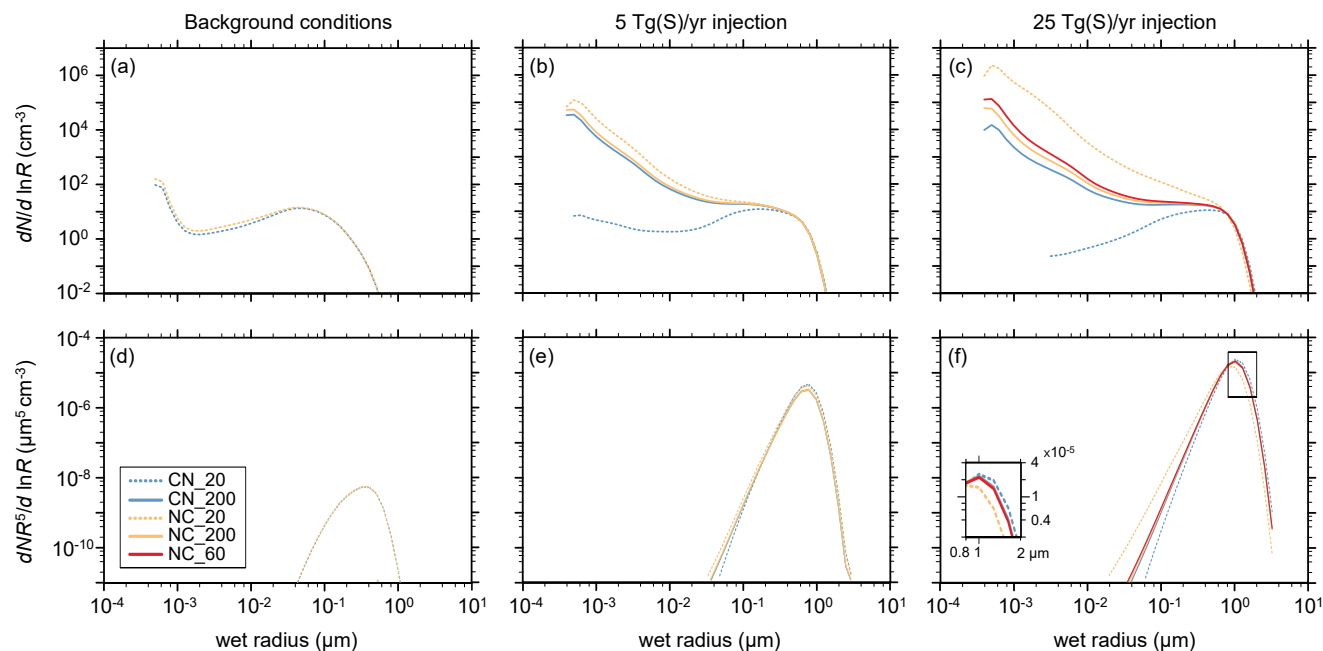


**Figure 2.** Upper row: Size distributions ( $dN/d \ln R$ , particles  $\text{cm}^{-3}$ ) averaged between  $30^\circ\text{S}$  and  $30^\circ\text{N}$  at 55 hPa for the model simulations with (a) stratospheric background conditions, (c) regional  $\text{SO}_2$  injections of  $5 \text{ Tg(S) yr}^{-1}$ , and (e)  $25 \text{ Tg(S) yr}^{-1}$ . Lower row: The fifth moment ( $dNR^5/d \ln R$ ,  $\mu\text{m}^5 \text{ cm}^{-3}$ ) of the aerosol size distributions as an estimate for aerosol sedimentation mass flux (particle volume ( $\propto R^3$ ) times sedimentation velocity ( $\propto R^2$ )). Blue lines: simulations with condensation first; orange and red lines: nucleation first. Dashed lines:  $N_{\text{micro}} = 20$  microphysical timesteps; solid orange and blue lines:  $N_{\text{micro}} = 200$ ; solid red lines in (e) and (f):  $N_{\text{micro}} = 60$ . Insert in (f) highlights the differences for coarse particles.

both microphysical settings, CN and CN, result in an average  $R_{\text{eff}}$  of  $0.15 \mu\text{m}$ . For the  $\text{SO}_2$  injections scenarios, most of the  
 240 additional sulfur condenses onto existing particles or is consumed in nucleation of new particles, which coagulate preferentially  
 into the range of optimal effective radius for scattering of solar radiation between  $0.3$  and  $0.4 \mu\text{m}$  (Weisenstein et al., 2022,  
 see their Fig. 4). The standard microphysical setup (CN,  $N_{\text{micro}} = 20$ , solid blue circles) result in the largest simulated  $R_{\text{eff}}$ , as  
 condensation partly suppresses the subsequent formation of smaller particles via nucleation. Conversely, nucleation first with  
 245 long microphysical timesteps (CN,  $N_{\text{micro}} = 20$ , solid orange circles) exaggerates the formation of small particles, resulting in  
 an underestimation of  $R_{\text{eff}}$ . Given a sufficiently short timestep ( $N_{\text{micro}} = 200$ ), CN and NC converge to  $R_{\text{eff}}$  of  $0.38 \mu\text{m}$   
 for the S5 scenario, and  $0.48 \mu\text{m}$  for the S25 scenario (blue and orange crosses). Compared to the modal models MAECHAM5-  
 HAM and CESM2, the sectional SOCOL-AER in general produces smaller  $R_{\text{eff}}$  for the regional injections. Hence, improving  
 the SOCOL-AER aerosol microphysics by swapping the sequence to nucleation first and increasing  $N_{\text{micro}}$  leads to a slight  
 250 reduction in the spread in  $R_{\text{eff}}$  among these models.

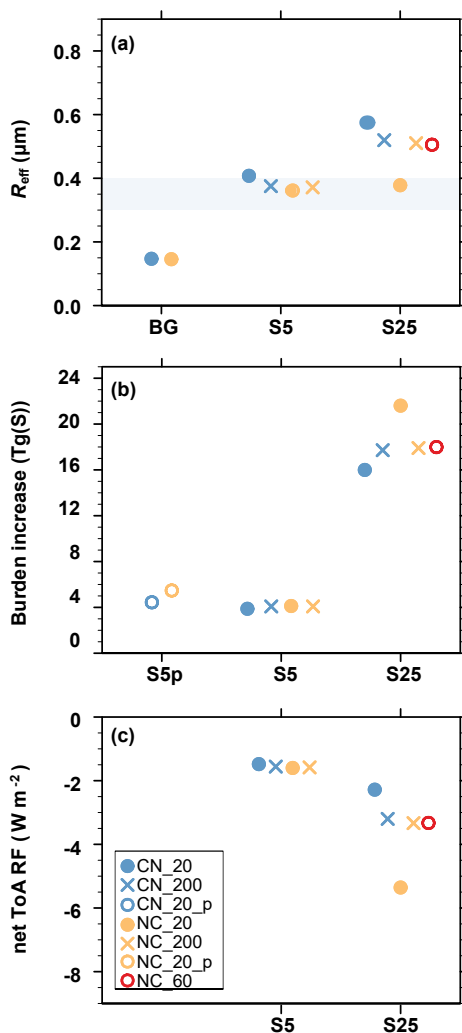


**Figure 3.** Effect of microphysical settings on the global averages of various calculated aerosol and radiative quantities. (a) Global mean effective radius ( $\mu\text{m}$ ) at 55 hPa. (b) Global mean sulfuric acid aerosol burden increase ( $\text{Tg(S)}$ ). (c) Global mean change in net top-of-atmosphere (shortwave + longwave) radiative forcing ( $\text{Wm}^{-2}$ ). Injection scenarios are: BG = background conditions (no injection); S5 =  $5 \text{ Tg(S) yr}^{-1}$  regional  $\text{SO}_2$  injection; S5p =  $5 \text{ Tg(S) yr}^{-1}$  point  $\text{SO}_2$  injection; and S25 =  $25 \text{ Tg(S) yr}^{-1}$  regional  $\text{SO}_2$  injection. Blue symbols: condensation first. Orange and red symbols: nucleation first. Open or filled circles:  $N_{\text{micro}} = 20$  (or 60). Crosses:  $N_{\text{micro}} = 200$ . Light blue shading in (a): optimal effective radii for scattering of solar radiation from Dykema et al. (2016) and Figure 4 in Weisenstein et al. (2022).

Figure 3b shows the impact of microphysical settings on the total (troposphere and stratosphere) aerosol burden increase in the intervention scenarios compared to background conditions. For background conditions, CN and CN with  $N_{\text{micro}} = 20$  show an almost identical aerosol burden (see also Table S1 in the Supplement). For the  $\text{SO}_2$  injection scenarios, the original



setup CN\_20 reveals the smallest aerosol burden. The largest aerosol burden is simulated by the simulation with CN\_20 setting,  
255 since this setup shifts the size distribution towards small particles, which have a longer stratospheric residence time. For the  
S5 scenario the dependence on call sequence is small, but for S25 the simulated aerosol burdens differ by more than 30%  
(Table S1). Despite this large spread in the simulated burden increase, SOCOL-AERv2 still falls between the CESM2 and  
the MAECHAM5-HAM models, which showed for most of the simulated injection scenarios the largest and smallest burden  
increase, respectively (Weisenstein et al., 2022, their Fig. 1).

260 Figure 3c displays globally averaged changes in the net top-of-atmosphere short- and longwave radiative forcing (RF) due to  
SO<sub>2</sub> injections. Since SOCOL-AERv2 uses prescribed SST and SIC, the climate intervention runs remain in non-equilibrium  
and the perturbation in radiative fluxes at TOA directly quantify the Effective RF (Forster et al., 2016). All S5 simulations  
show a rather consistent RF change of around  $-1.5 \text{ W m}^{-2}$ . For the S25 simulations, however, we find a large spread in RF,  
ranging from  $-2.3 \text{ W m}^{-2}$  for the original microphysical setup (CN\_20) to  $-5.4 \text{ W m}^{-2}$  for the simulation with reversed call  
265 sequence (CN\_20). As already mentioned in Weisenstein et al. (2022), the differences in RF between the various SOCOL-  
AERv2 simulations, but also between different models, are mainly related to the respective burden increases (Fig. 3b). The  
simulations with the largest burden increase also show the smallest  $R_{\text{eff}}$ , which efficiently scatters the incoming solar radiation  
and enhances the negative RF.

As discussed in previous studies (Heckendorn et al., 2009; Kleinschmitt et al., 2018), the efficacy of the SO<sub>2</sub> injection,  
270 i.e. the RF per Tg of sulfur injected annually, decreases with increasing injection rate, since the aerosol particles grow larger,  
which increases sedimentation and decreases scattering efficiency. However, the model intercomparison by Weisenstein et al.  
(2022) revealed that not only the radiative efficacy itself, but also its decrease with increasing injection rates is strongly  
model dependent. For SOCOL in Fig. 3c, the radiative efficacy of the various S5 simulations ranges moderately between  
 $-0.28$  and  $-0.34 \text{ W m}^{-2} (\text{Tg(S) yr}^{-1})^{-1}$ . For the S25 simulations, the simulations with highest and lowest efficacy differ  
275 by more than a factor of 2. The applied microphysical improvements lead to a significantly higher radiative efficacy ( $0.09$   
 $\text{W m}^{-2} (\text{Tg(S) yr}^{-1})^{-1}$  for S25\_CN\_60) compared to the default setup ( $0.13 \text{ W m}^{-2} (\text{Tg(S) yr}^{-1})^{-1}$  for S25\_CN\_20).

As SOCOL-AERv2 does not include an interactive ocean model, but prescribed SSTs, it is unfeasible to test the impact  
of the call sequence on surface temperature anomalies. To overcome this limitation, we performed the G4 GeoMIP scenario  
with the CN setup (S5p\_CN\_20) using the ESM SOCOLv4, a coupled model which shares the same exact aerosol module  
280 as SOCOL-AERv2 (see methods). In this model, we use point injections, in keeping with the G4 protocol (see section 2.3).  
The simulation shows an increase of 25% in stratospheric aerosol burden compared to the conventional S5p\_CN\_20 scenario  
(see Fig. 3b, left). The corresponding global averaged surface cooling is 0.65 K and 1.02 K for S5p\_CN\_20 and S5p\_CN\_20,  
respectively, which is an increase of 57%, whereas no significant differences in global stratospheric aerosol burden and RF  
were found among regional S5 scenarios performed with SOCOL-AERv2 (see Fig. 3b, middle). This underlines the sensitivity  
285 of our results to the chosen injection scenario (point vs. regional) as well as to the model resolution (section 2.2). Both the  
model resolution and the injection scenario can lead to locally very different H<sub>2</sub>SO<sub>4</sub> supersaturation.



### 3.3 Influence of settings on meridional distributions of aerosol burden, radiative forcing, and ozone

Figure 4a,b show the influence of microphysical settings on the modeled latitudinal variation of the sulfate aerosol column burden (stratosphere plus troposphere) for the climate intervention scenarios simulated with SOCOL-AERv2 (S5 and S25). In contrast, background simulations (not shown) have almost no dependence on the call sequence (see Table S1 in the Supplement). The SO<sub>2</sub> injection scenarios show similar latitudinal patterns, with aerosol column burdens peaking over the inner tropics, confined by the tropical leaky pipe. After overcoming the subtropical jet, the burden again maximizes around 45°N/S in the stratospheric surf zone, whereas the polar regions are isolated by the polar jets. As discussed before (Fig. 3b), the original setting CN<sub>20</sub> results in the smallest aerosol burden, whereas CN<sub>20</sub> with "nucleation first" shifts the size distribution towards smaller particles with less gravitational settling (see also Table S1).

The latitudinal variations of the radiative forcing (RF) in Fig. 4c,d show the mirror image of the burden in Fig. 4a,b, with reduced irradiance at high aerosol loading, and illustrate the direct radiative effects of the aerosol. However, in contrast to the smooth distributions of aerosol loading, RF exhibits a much higher degree of small fluctuations due to tropospheric cloud variability. The latitudinal variations in RF are very similar for all S5 simulations and the S25 simulations also show a consistent geographic pattern. The negative RF covers more than 80% of the globe, with the exception of the polar caps where absorption of outwelling infrared radiation by the aerosol predominates and the RF becomes positive. The differences between the individual simulations become largest in the tropics, reflecting the sensitivity of the aerosol loading to the microphysical setup.

Figure 4e,f shows the impact of the simulated SO<sub>2</sub> injections on zonally averaged total column ozone as difference to the reference simulation BG\_CN<sub>20</sub>. As already discussed by Weisenstein et al. (2022), the SO<sub>2</sub> injections lead to a massive reduction of the ozone column. This is caused by accelerated ClO<sub>x</sub>-induced and HO<sub>x</sub>-induced ozone destruction cycles, which in turn are due to heterogeneous N<sub>2</sub>O<sub>5</sub> hydrolysis on the aerosol particles (leaving less NO<sub>2</sub> required for ClO<sub>x</sub> and HO<sub>x</sub> deactivation). The N<sub>2</sub>O<sub>5</sub> hydrolysis rate is proportional to the SAD (see next section and Figs. S2 and S3 in the Supplement). Both injection scenarios, S5 and S25, show similar patterns with the most pronounced changes in mid- to high latitudes. In the polar regions, the ozone loss is mainly caused by enhanced heterogeneous ClONO<sub>2</sub> activation on the additional aerosol SAD. Furthermore, in agreement with the CESM2 model, SOCOL-AER simulates a decrease of the ozone column in the tropics, where the accelerated Brewer-Dobson circulation leaves less time for ozone formation by molecular oxygen photolysis. In the tropics, the presented microphysical modifications do not show any significant impact on the simulated ozone decrease (Fig. 4e and f), despite clear differences in the simulated SAD for the same sulfur injection (Figs. S2 and S3). This result indicates that above a certain threshold a further SAD increase does not affect the NO<sub>x</sub> cycle and its coupling to the ClO<sub>x</sub> and HO<sub>x</sub> cycles anymore. The fact that the S25 simulations result in a more pronounced total column ozone change than the S5 simulations is related to a more pronounced strengthening of the Brewer-Dobson circulation, which reduces the time for chemical ozone formation, and the increased stratospheric H<sub>2</sub>O entry, which enhances ozone loss by the HO<sub>x</sub> cycle (Tilmes et al., 2018).

In mid- to high latitudes both injection scenarios, S5 and S25, reveal substantial differences in the total ozone loss simulated, depending on the microphysical settings used in the simulations. For the S5 simulations (Fig. 4e), the total ozone losses over



Antarctica range between 24 and 30 DU. For the Northern Hemisphere, the spread in simulated polar ozone losses is with 6 to 24 DU even larger. For the S25 simulations (Fig. 4e and f), the simulated polar ozone loss range between 60 and 80 DU over the Southern Hemisphere, and between 35 and 60 DU over the Northern Hemisphere. It should be noted that the microphysical setup with the smallest ozone change in one hemisphere, does not necessarily also show the smallest ozone change on the other hemisphere, which might be related to the dynamical variability.

It should be emphasized that the discussed changes in total column ozone caused by stratospheric SO<sub>2</sub> injections refer to stratospheric concentrations of ozone depleting substances and GHGs projected for the year 2040. With further decreasing stratospheric chlorine loadings in the future, the impact of the enhanced aerosol SAD under SO<sub>2</sub> injections on total column ozone might change as the coupling between the ClO<sub>x</sub> and NO<sub>x</sub> cycle becomes less important.

### 3.4 Influence of settings on SAD and stratospheric temperature

Climate intervention by stratospheric SO<sub>2</sub> emission yields an increase in aerosol surface area density (SAD), which enables heterogeneous chemical reactions such as N<sub>2</sub>O<sub>5</sub> hydrolysis, but which is also an approximate measure of the extinction and, hence, the backscatter of shortwave radiation. Moreover, the aqueous H<sub>2</sub>SO<sub>4</sub> aerosol absorbs outwelling longwave radiation, which increases the air temperature, with repercussions for stratospheric dynamics.

Both quantities, SAD and temperature, are also affected by the microphysical settings CN versus CN and  $N_{\text{micro}}$ . In brief, the CN setting with  $N_{\text{micro}} = 200$  yields higher SAD than CN with  $N_{\text{micro}} = 20$ , roughly by 20%. This is due to the smaller particles with higher SAD and larger burden (see Figs. S2 and S3 in the Supplement). The larger burden, in turn, leads to more longwave radiative heating, which increases stratospheric temperatures. This is a marginal effect in the S5 scenario, but corresponds to about 1 K higher temperatures under S25 conditions (see Fig. S4 in the Supplement). A strongly temperature dependent reaction such as O<sub>3</sub> + O → 2 O<sub>2</sub> changes by about 4% for Δ*T* = 1 K, so that the impact of microphysical settings on ozone via SAD-changes is by far more important than the impact via *T*-changes. Also differences from dynamical feedbacks between the different settings are likely small since the absolute temperature increase from the S25 scenarios is up to 15 K and thus much larger.

### 3.5 Influence of settings on modeling the eruption of Mt. Pinatubo

So far, our study has highlighted the impacts of the microphysical settings for an extreme case involving climate intervention. Here, we expand this analysis, by evaluating the effects under conditions of volcanic eruptions on the 1991 eruption of Mt. Pinatubo by using the PIN\_CN\_20, PIN\_CN\_20 and the PIN\_CN\_200 settings (Table 1). We compared the evolution of the computed global stratospheric aerosol burden with SAGE and HIRS satellite data and the evolution of the computed mean effective particle radius with balloon measurements over Laramie (Wyoming, see Fig. 5). Details on the observational data sets and their uncertainties as well as model and inter-model uncertainties can be found in Sukhodolov et al. (2018) and Quaglia et al. (2023). All model settings show a very similar peak in the stratospheric aerosol burden, but distinctly different declines during the years 1992/93. "Nucleation first" shifts the size distribution towards smaller particles, which have a longer stratospheric residence time. The slower decline is in better agreement with observations, although it should be mentioned that

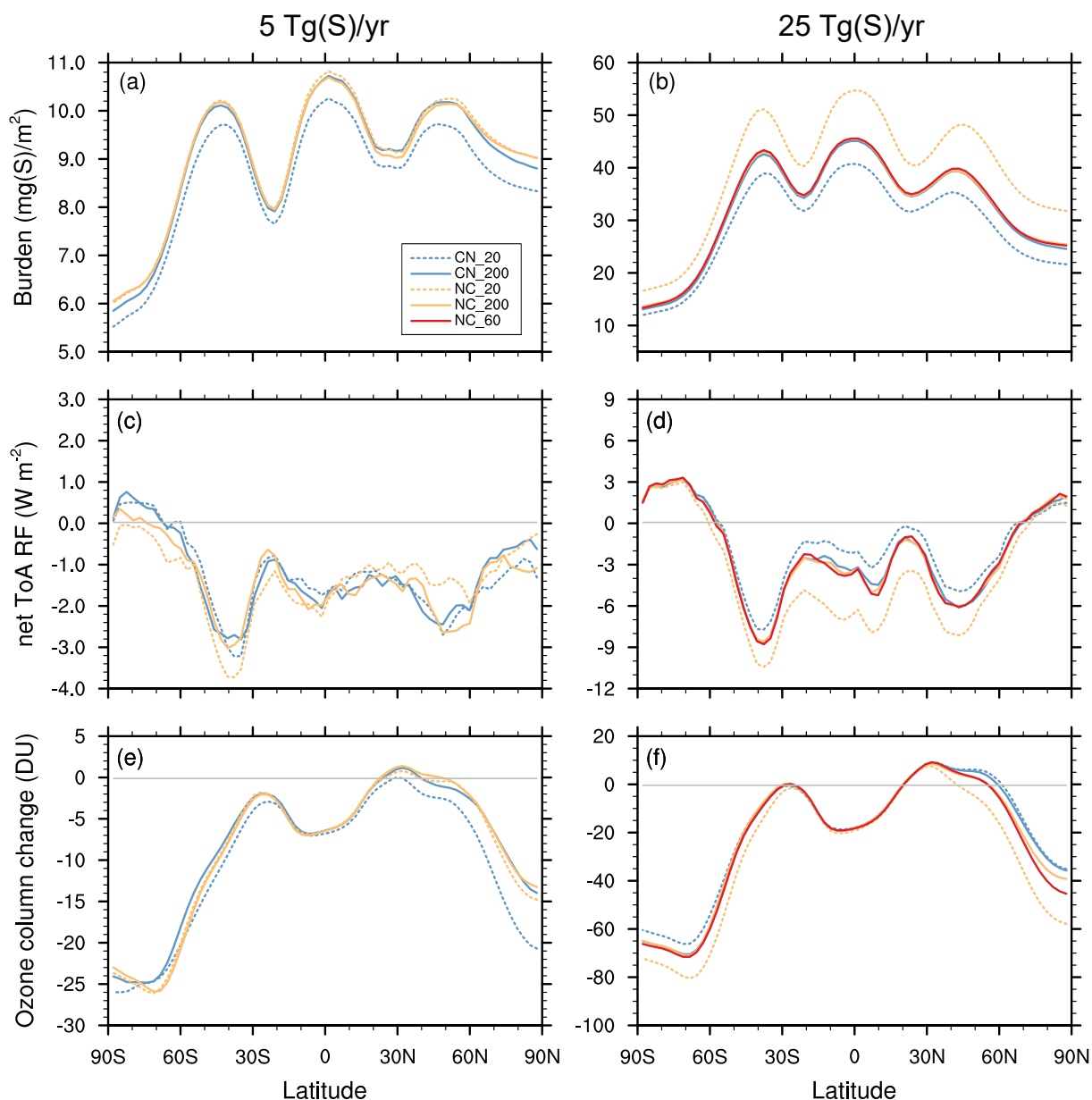


**Figure 4.** Effect of microphysical settings on the zonal averages of various calculated aerosol, radiative and chemical quantities. Left column: regional  $\text{SO}_2$  injections of  $5 \text{ Tg(S) yr}^{-1}$ . Right column: regional  $\text{SO}_2$  injections of  $25 \text{ Tg(S) yr}^{-1}$ . **(a,b)** Sulfuric acid aerosol burden per square meter ( $\text{mg(S) m}^{-2}$ ). **(c,d)** Zonal mean net top-of-atmosphere (shortwave + longwave) radiative forcing ( $\text{Wm}^{-2}$ ). **(e,f)** Change in zonal average column ozone (Dobson units). Blue lines: simulations with condensation first; orange and red lines: nucleation first. Dashed lines:  $N_{\text{micro}} = 20$  microphysical timesteps; solid orange and blue lines:  $N_{\text{micro}} = 200$ ; solid red lines:  $N_{\text{micro}} = 60$ . All panels use the simulation BG\_CN\_20 as reference.





the agreement with observations strongly depends on the assumed  $\text{SO}_2$  emissions profile (Quaglia et al., 2023). Regarding the  
355 mean  $R_{\text{eff}}$ , PIN\_CN\_20 simulates smaller values than PIN\_CN\_20 for the first couple of months after the eruption and higher  
values later on, as PIN\_CN\_20 returns faster towards background conditions due to faster sedimentation of larger particles.  
Overall, the microphysical modifications do not overly influence the discrepancy between modeled and observed  $R_{\text{eff}}$  (Fig. 5b).

However, other than under climate intervention conditions the evolution of the aerosol burden and  $R_{\text{eff}}$  in the PIN\_CN\_20  
scenario are much closer to PIN\_CN\_20 than to PIN\_CN\_20. The volcanic eruption is a point event in time and space, whereas  
360 the geoengineering scenarios have continuous emissions across all longitude and  $30^\circ\text{N}$  and  $30^\circ\text{S}$  in latitude, which establish a  
steady-state situation. This leads to  $\text{H}_2\text{SO}_4$  production rates, which locally are about  $10^4$ - $10^5$  times larger in the Mt.  
Pinatubo case compared to S5 and S25. Since nucleation is exponentially dependant on the  $\text{H}_2\text{SO}_4$  supersaturation this leads to  
erroneously large nucleation rates in the PIN\_CN\_20 scenario. Coagulation is not efficient enough to remove the large amount  
of nucleation mode particles in that scenario. When increasing  $N_{\text{micro}}$  to 200 (PIN\_CN\_200) the burden and the  $R_{\text{eff}}$  of the  
365 plume evolve following the PIN\_CN\_20 scenario since local supersaturations are smaller now and coagulation can keep up with  
efficiently removing the nucleation mode particles.

Therefore, for volcanic eruptions, where  $\text{H}_2\text{SO}_4$  supersaturations are locally much larger compared to climate engineering  
scenarios, the correct solution is much closer to CN\_20, since otherwise nucleation would erroneously dominate over con-  
densation. This is a good example how the very different distributions of  $\text{H}_2\text{SO}_4$  supersaturation in space and time when  
370 simulating volcanic eruptions and geoengineering scenarios lead to different challenges within aerosol microphysics schemes  
(Heckendorn et al., 2009; Vattioni et al., 2019).

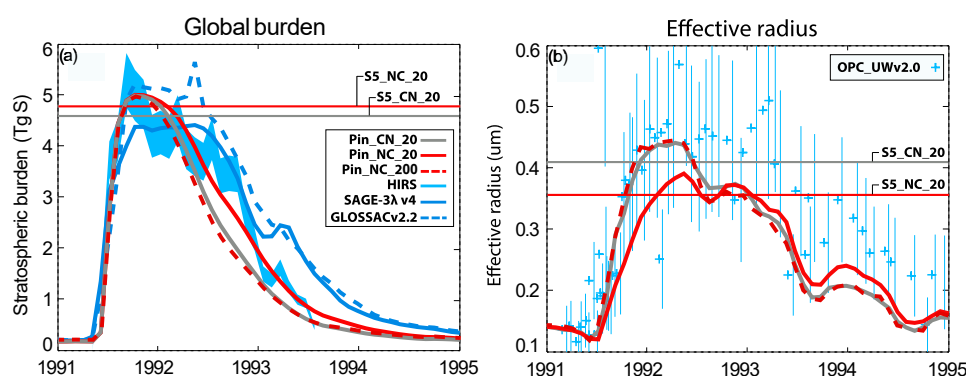


**Figure 5.** (a) Evolution of the simulated global stratospheric aerosol burden (Tg(S)) for PIN\_CN\_20 and PIN\_CN\_20 compared with HIRS- and SAGE-II-derived data (SAGE-3,4λ and GLOSSACv2.2, Arfeuille et al., 2013; Thomason et al., 2018; Kovilakam et al., 2020). HIRS-derived total (troposphere and stratosphere) aerosol sulfur burden assumes 75% sulfuric acid by weight (Baran and Foot, 1994). Light blue shaded area: uncertainties of HIRS. (b) Effective particle radius ( $\mu\text{m}$ ) averaged over the altitude range from 14 to 30 km compared to in-situ measurements taken at Laramie, Wyoming (OPC UWv2.0, Deshler et al., 2019). Thin blue whiskers reflect the measurement uncertainty (adapted from Quaglia et al., 2023). For comparison the steady-state values for S5\_CN\_20 and S5\_CN\_20 from this work are shown as thin horizontal red and gray lines in both panels.



#### 4 Comparison with other work and conclusions

In this study, we have shown the importance of properly setting the length of the microphysical timestep and the call sequence of nucleation and condensation for modeling the global stratospheric sulfuric acid aerosol under conditions of SO<sub>2</sub> injections for climate engineering. In the aerosol-chemistry-climate model SOCOL-AERv2, the evolution of the H<sub>2</sub>SO<sub>4</sub> concentration in the gas-phase is determined by sequential operator splitting using a sub-stepping approach for aerosol microphysics with a default timestep of 6 min, i.e. the H<sub>2</sub>SO<sub>4</sub> gas-phase concentration is consecutively updated by H<sub>2</sub>SO<sub>4</sub> production from chemistry, condensation and nucleation. We found the following:

- Under stratospheric background conditions, the call sequence does not affect the model results, indicating that the default number of microphysical sub-timesteps is sufficient to prevent the first called process from spuriously dominating the size distribution.
- Under elevated H<sub>2</sub>SO<sub>4</sub> supersaturations in the stratosphere the characteristic times for nucleation and condensation may become shorter than the default microphysical timestep. In such cases, the competition between the two H<sub>2</sub>SO<sub>4</sub> sinks affects the simulated aerosol size distribution and the microphysical time step must be reduced.
- The default setting "condensation first" can massively underestimate the fraction of nucleation mode particles, whereas "nucleation first" tends to underestimate the number of coarse mode particles. Tests of numerical convergence with very short timesteps indicate that "nucleation first" yields smaller numerical errors for regional SO<sub>2</sub> injections, whereas condensation first yields smaller numerical errors for the simulation of volcanic eruptions with locally and temporally extremely high H<sub>2</sub>SO<sub>4</sub> supersaturations.
- Despite significant shifts in simulated aerosol size distributions, the main response patterns of atmospheric chemistry and climate to stratospheric SO<sub>2</sub> injections as simulated with SOCOL-AERv2 are robust to microphysical time integration adjustments, but the strength of the response can differ substantially in the case of high injection rates (such as 25 Tg(S) yr<sup>-1</sup>) or point injections (such as 5 Tg(S) yr<sup>-1</sup> point injections, S5p), which both lead to large H<sub>2</sub>SO<sub>4</sub> supersaturations.
- The radiative forcing found for the 25 Tg(S) yr<sup>-1</sup> injection scenario varies by more than a factor of 2 between the different microphysical settings. Nevertheless, this model-internal uncertainty in SOCOL-AERv2 is still smaller than the scatter between the three GCMs with interactive aerosol microphysics – CESM2-WACCM6, MAECHAM5-HAM, and SOCOL-AERv2 – compared by Weisenstein et al. (2022) in strictly coordinated climate intervention modeling.

The first part of our conclusions confirms the study by Wan et al. (2013), who investigated different time integration methods to solve the H<sub>2</sub>SO<sub>4</sub> continuity equation using two versions of the ECHAM-HAM model: HAM1 with an Euler forward scheme with sequential operator splitting similar to SOCOL-AERv2, but without microphysical substeps; HAM2 with a two-step time integration scheme implemented by Kokkola et al. (2009). They identified sequential operator splitting with too long timesteps as major source of numerical error in HAM1, and proposed simultaneous processing of condensation and nucleation to better



represent the competition between both processes. The microphysical sub-stepping technique as applied in SOCOL-AERv2  
405 improves the results of the operator splitting approach, but requires a sufficiently large number of substeps. Instead of using a  
fixed number of substeps, a dynamical timestep adjustment could be beneficial, but we have not tested this here.

The importance of aerosol microphysics and the competition between nucleation and condensation on the simulated aerosol  
size distribution and the radiative efficiency of stratospheric sulfur injections was also shown by Laakso et al. (2022), who in-  
vestigated different injection strategies using the ECHAM-HAMMOZ model with two different aerosol schemes, the sectional  
410 SALSA scheme as well as the modal M7 scheme. SALSA describes the aerosol size distribution in 10 size bins, while M7  
uses 7 lognormal modes. The authors found that nucleation of new particles dominates over condensational particle growth in  
the sectional SALSA scheme, while the opposite is the case in the modal M7 module. In addition, the use of lognormal modes  
results in a minimum in the particle size distribution in the optimal size range for solar scattering and restricts the growth of  
particles in accumulation mode, tending to underestimate gravitational settling. These differences resulted in smaller particles  
415 in SALSA and, therefore, a higher radiative forcing. For an injection scenario of  $20 \text{ Tg(S) yr}^{-1}$ , SALSA revealed a global net  
ToA radiative forcing of around  $8 \text{ W m}^{-2}$ , M7 resulted in  $3 \text{ W m}^{-2}$ . This spread is even larger than what we found for the  
S25 simulations S25\_CN\_20 and S25\_CN\_20. Laakso et al. (2022) further investigated the impact of the competition between  
nucleation and condensation by performing simulations with the nucleation being switched off in both aerosol modules by  
emitting 25% of the sulfur directly as 3 nm particles. The results of these sensitivity studies indicate that the different treat-  
420 ment of nucleation and condensation explains the differences in radiative forcing between SALSA and M7 only partly: The  
difference in radiative forcing was reduced from  $5 \text{ W m}^{-2}$  to about  $3 \text{ W m}^{-2}$ .

Apart from time integration or representation of the aerosol size distribution, numerical parameterizations of individual  
processes are another source of uncertainty. The binary-homogeneous nucleation scheme by Vehkamäki et al. (2002), for  
example, is widely used in models, including SOCOL-AERv2 or the above mentioned aerosol schemes SALSA and M7.  
425 The latter two include an extension of the scheme for high sulfate concentrations implemented by Kokkola et al. (2009),  
using the collision rate as maximum possible nucleation rate. In a very recent study, Yu et al. (2023) evaluated simulated  
nucleation rates in the lowermost stratosphere by CLOUD laboratory measurements under stratospheric temperatures. They  
found that the Vehkamäki scheme overestimates observed nucleation rates by 3 to 4 orders of magnitude. As the particle size  
distribution is not only determined by nucleation, but also by particle growth through condensation and coagulation, Yu et al.  
430 (2023) compared the simulated size distributions to in-situ measurements of the particle number densities down to a diameter  
of 3 nm obtained during the NASA Atmospheric Tomography Mission (ATom) between 2016 and 2018. In the size range  
between 3 to 10 nm, the number densities simulated with the GEOS-Chem model using the Vehkamäki et al. scheme were  
1-2 orders of magnitude higher than observed. The same holds true for SOCOL-AERv2: under background conditions in the  
southern hemisphere lowermost stratosphere ( $70^\circ \text{S}$ , 12 km altitude), modeled number densities for particles smaller than  
435 10 nm in diameter range between  $10^3$  and  $10^4 \text{ cm}^{-3}$ , while the ATom observations indicate values between slightly below  
 $10^1$  to  $10^2 \text{ cm}^{-3}$ . Using the kinetic scheme for ion-mediated and binary homogeneous nucleation (Yu et al., 2020) calculated  
nucleation rates, but also the size distributions simulated by GEOS-Chem were closer to ATom. Furthermore, the results by Yu  
et al. (2023) suggest that under low stratospheric background  $\text{H}_2\text{SO}_4$  concentrations nucleation on ions, which is usually not



represented in global models, dominates over binary homogeneous  $\text{H}_2\text{SO}_4\text{-H}_2\text{O}$  nucleation. However, the importance of binary  
440 homogeneous nucleation is expected to increase under high  $\text{H}_2\text{SO}_4$  concentrations. Unfortunately, CLOUD measurements of  
nucleation rates refer to stratospheric background conditions only and do not cover strongly elevated  $\text{H}_2\text{SO}_4$  concentrations  
under  $\text{SO}_2$  injection scenarios or after volcanic eruptions, but based on the findings of Yu et al. (2023) it may be that all  
models using the Vehkamäki scheme overestimate the role of nucleation. This might explain the low bias in the simulated  
mean effective radius compared to in-situ measurements following the eruption of Mt. Pinatubo. Furthermore, this might  
445 have substantial repercussions on the simulated aerosol size distribution, aerosol burdens and radiative forcing under climate  
intervention conditions, most likely resulting in a decreased efficiency of  $\text{SO}_2$  injections.

This work adds to a series of recent publications that highlight the crucial role of aerosol microphysics for simulated aerosol  
properties and modeled estimates of geoengineering effects on atmospheric chemistry and climate. Our results clearly demon-  
strate that there is considerable uncertainty when numerical schemes like the aerosol microphysics in SOCOL-AERv2 are  
450 applied under unprecedented conditions, such as stratospheric solar geoengineering with continuously large  $\text{SO}_2$  emissions,  
even if these models had been thoroughly evaluated and are well capable of reproducing observations under background or  
moderately perturbed conditions like volcanic eruptions. It should be emphasized that our conclusions are mainly based on  
simulations of regional  $\text{SO}_2$  injections, which are supported by point injection scenarios and simulations of the 1991 Mt.  
Pinatubo eruption. As the nucleation rate strongly depends on the gas-phase  $\text{H}_2\text{SO}_4$  concentration, ambient temperatures and  
455 relative humidities, the optimal number of microphysical (sub-)timesteps will depend on the assumed  $\text{SO}_2$  injection rates, but  
also on the injection scenario and region. Point injections of  $\text{SO}_2$ , for example result in very high, but locally confined  $\text{H}_2\text{SO}_4$   
supersaturations, potentially making the results more sensitive to the details of the microphysical approach. The intention of  
this paper is to raise awareness within the (aerosol) modelling community for potential numerical problems within conventional  
aerosol microphysics modules when applying them to unprecedented extreme conditions such as high  $\text{H}_2\text{SO}_4$  supersaturations  
460 from  $\text{SO}_2$  injection for climate intervention.

While this study focused on the importance of a proper temporal resolution of aerosol microphysics, it did not address ef-  
fects of spatial resolution. Properly resolving the various temporal and spatial scales, ranging from nanometers and seconds for  
microphysical processes to kilometers and decades for global climate, remains a significant challenge for aerosol-chemistry-  
climate models (Vattioni et al., 2019; Weisenstein et al., 2022). Continuous model development, such as embedded  $\text{SO}_2$  emis-  
465 sion plume modelling (Sun et al., 2022), is indispensable to close the spatial and temporal gap between aircraft emission  
plumes and large-scale model grids, and to effectively reduce existing model uncertainties with respect to the effectiveness of  
geoengineering by stratospheric sulfur injections. Furthermore, additional laboratory or small-scale field studies of aerosol for-  
mation, growth and dispersion under various stratospheric conditions could also be beneficial to evaluate and improve existing  
numerical models.



470 *Supplement.* The supplement related to this article is available online at <https://doi.org/10.5194/amt-16-xxx-2023-supplement>.

*Code and data availability.* The original SOCOL-AERv2 code is available at <https://doi.org/10.5281/zenodo.5733121> (Brodowsky et al., 2018). The simulation data using that model code, which does not account for the interpolation of H<sub>2</sub>SO<sub>4</sub> production within the microphysical subloop are available at <https://doi.org/10.3929/ethz-b-000610854> (Stenke et al., 2023). The modified source code of SOCOL-AERv2 handling the microphysical subloop by taking into account the interpolation of H<sub>2</sub>SO<sub>4</sub> production within the  
475 microphysical subloop as well as the data from these simulations are available at <http://hdl.handle.net/20.500.11850/622193> (Vattioni et al., 2023).

*Author contributions.* SV proposed the study and implemented the modifications to the microphysical scheme. SV and AS performed the geoengineering simulations with SOCOL-AERv2 and analysed the model results. EW performed and analyzed the simulations with SOCOLv4. TS conducted and analyzed the Pinatubo simulations. Significant scientific guidance on the overall project was provided by TP  
480 and BL. AS drafted a first version of the manuscript. All co-authors contributed to the discussion and the text.

*Competing interests.* At least one of the (co-)authors is a member of the editorial board of Geoscientific Model Development. Other than this, the authors declare that they have no conflict of interest.

*Acknowledgements.* Our special thanks go to Debra Weisenstein for discussions about the original AER code. We also thank Ilaria Quaglia for providing the processed OPC data. Support for Gabriel Chiodo and Andrea Stenke was provided by the Swiss Science Foundation  
485 within the Ambizione grant no. PZ00P2\_180043. Support for Sandro Vattioni was provided by the ETH Research grant no. ETH-1719-2 as well as by the Harvard Geoengineering Research Program. Timofei Sukhodolov acknowledges the support from the Swiss National Science Foundation (grant no. 200020-182239) and the Karbacher Fonds, Graubünden, Switzerland.



## References

- Arfeuille, F., Luo, B. P., Heckendorn, P., Weisenstein, D., Sheng, J. X., Rozanov, E., Schraner, M., Brönnimann, S., Thomason, L. W., and  
490 Peter, T.: Modeling the stratospheric warming following the Mt. Pinatubo eruption: uncertainties in aerosol extinctions, *Atmos. Chem.  
Phys.*, 13, 11 221–11 234, <https://doi.org/10.5194/acp-13-11221-2013>, 2013.
- Ayers, G., Gillett, R., and Gras, J.: On the vapor pressure of sulfuric acid, *Geophys. Res. Lett.*, 7, 433–436,  
<https://doi.org/10.1029/GL007i006p00433>, 1980.
- Baran, A. J. and Foot, J. S.: New application of the operational sounder HIRS in determining a climatology of sulphuric acid aerosol from  
495 the Pinatubo eruption, *J. Geophys. Res.*, 99, 25 673–25 679, <https://doi.org/10.1029/94JD02044>, 1994.
- Brodowsky, C. et al.: SOCOL-AERv2 model code, Zenodo, <https://doi.org/10.5281/zenodo.5733121>, 2018.
- Budyko, M. I.: *Climate and Life*, Academic Press, New York, USA, 1974.
- Crutzen, P.: Albedo Enhancement by Stratospheric Sulfur Injections: A Contribution to Resolve a Policy Dilemma?, *Climatic Change*, 77,  
211–220, <https://doi.org/10.1007/s10584-006-9101-y>, 2006.
- 500 Danabasoglu, G., Lamarque, J.-F., Bacmeister, J., Bailey, D. A., DuVivier, A. K., Edwards, J., Emmons, L. K., Fasullo, J., Garcia, R.,  
Gettelman, A., Hannay, C., Holland, M. M., Large, W. G., Lauritzen, P. H., Lawrence, D. M., Lenaerts, J. T. M., Lindsay, K., Lipscomb,  
W. H., Mills, M. J., Neale, R., Oleson, K. W., Otto-Bliesner, B., Phillips, A. S., Sacks, W., Tilmes, S., van Kampenhou, L., Vertenstein,  
M., Bertini, A., Dennis, J., Deser, C., Fischer, C., Fox-Kemper, B., Kay, J. E., Kinnison, D., Kushner, P. J., Larson, V. E., Long, M. C.,  
Mickelson, S., Moore, J. K., Nienhouse, E., Polvani, L., Rasch, P. J., and Strand, W. G.: The Community Earth System Model Version 2  
505 (CESM2), *Journal of Advances in Modeling Earth Systems*, 12, e2019MS001 916,  
<https://doi.org/https://doi.org/10.1029/2019MS001916>, 2020.
- Deshler, T., Luo, B., Kovilakam, M., Peter, T., and Kalnajs, L. E.: Retrieval of Aerosol Size Distributions From In Situ Particle Counter  
Measurements: Instrument Counting Efficiency and Comparisons With Satellite Measurements, *Journal of Geophysical Research:  
Atmospheres*, 124, 5058–5087, <https://doi.org/10.1029/2018JD029558>, 2019.
- 510 Dykema, J. A., Keith, D. W., and Keutsch, F. N.: Improved aerosol radiative properties as a foundation for solar geoengineering risk  
assessment, *Geophysical Research Letters*, 43, 7758–7766, <https://doi.org/https://doi.org/10.1002/2016GL069258>, 2016.
- Egorova, T., Rozanov, E., Zubov, V., and Karol, I. L.: Model for Investigating Ozone Trends (MEZON), *Izvestiya, Atmos. Oceanic Phys.*,  
39, 277–292, 2003.
- English, J. M., Toon, O. B., Mills, M. J., and Yu, F.: Microphysical simulations of new particle formation in the upper troposphere and  
515 lower stratosphere, *Atmos. Chem. Phys.*, 11, 9303–9322, <https://doi.org/10.5194/acp-11-9303-2011>, 2011.
- Feinberg, A., Sukhodolov, T., Luo, B.-P., Rozanov, E., Winkel, L. H. E., Peter, T., and Stenke, A.: Improved tropospheric and stratospheric  
sulfur cycle in the aerosol–chemistry–climate model SOCOL-AERv2, *Geosci. Model Dev.*, 12, 3863–3887,  
<https://doi.org/10.5194/gmd-12-3863-2019>, 2019.
- Forster, P. M., Richardson, T., Maycock, A. C., Smith, C. J., Samset, B. H., Myhre, G., Andrews, T., Pincus, R., and Schulz, M.:  
520 Recommendations for diagnosing effective radiative forcing from climate models for CMIP6, *Journal of Geophysical Research:  
Atmospheres*, 121, 12–460, 2016.
- Fuchs, N.: *The Mechanics of Aerosols*, Pergamon Press, Oxford, 1964.



- Heckendorn, P., Weisenstein, D., Fueglistaler, S., Luo, B. P., Rozanov, E., Schraner, M., Thomason, L. W., and Peter, T.: The impact of geoengineering aerosols on stratospheric temperature and ozone, *Environ. Res. Lett.*, 4, 045 108, <https://doi.org/10.1088/1748-9326/4/4/045108>, 2009.
- 525 Jacob, D. J.: Chemistry of OH in remote clouds and its role in the production of formic acid and peroxymonosulfate, *J. Geophys. Res.*, 91, 9807–9826, <https://doi.org/10.1029/JD091iD09p09807>, 1986.
- Jacobson, M. Z. and Seinfeld, J. H.: Evolution of nanoparticle size and mixing state near the point of emission, *Atmos. Environ.*, 38, 1839–1850, <https://doi.org/10.1016/j.atmosenv.2004.01.014>, 2004.
- 530 Jungclaus, J. H., Fischer, N., Haak, H., Lohmann, K., Marotzke, J., Matei, D., Mikolajewicz, U., Notz, D., and von Storch, J. S.: Characteristics of the ocean simulations in the Max Planck Institute Ocean Model (MPIOM) the ocean component of the MPI-Earth system model, *Journal of Advances in Modeling Earth Systems*, 5, 422–446, <https://doi.org/https://doi.org/10.1002/jame.20023>, 2013.
- Kasten, F.: Falling speed of aerosol particles, *J. Appl. Meteorol.*, 7, 944–947, [https://doi.org/10.1175/1520-0450\(1968\)007<0944:FSOAP>2.0.CO;2](https://doi.org/10.1175/1520-0450(1968)007<0944:FSOAP>2.0.CO;2), 1968.
- 535 Kleinschmitt, C., Boucher, O., and Platt, U.: Sensitivity of the radiative forcing by stratospheric sulfur geoengineering to the amount and strategy of the SO<sub>2</sub> injection studied with the LMDZ-S3A model, *Atmos. Chem. Phys.*, 18, 2769–2786, <https://doi.org/10.5194/acp-18-2769-2018>, 2018.
- Kokkola, H., Hommel, R., Kazil, J., Niemeier, U., Partanen, A.-I., Feichter, J., and Timmreck, C.: Aerosol microphysics modules in the framework of the ECHAM5 climate model – intercomparison under stratospheric conditions, *Geosci. Model Dev.*, 2, 97–112, <https://doi.org/10.5194/gmd-2-97-2009>, 2009.
- 540 Kovilakam, M., Thomason, L. W., Ernest, N., Rieger, L., Bourassa, A., and Millán, L.: The Global Space-based Stratospheric Aerosol Climatology (version 2.0): 1979–2018, *Earth. Syst. Sci. Data*, 12, 2607–2634, doi: 10.5194/essd-12-2607-2020, 2020.
- Kravitz, B., Robock, A., Boucher, O., Schmidt, H., Taylor, K. E., Stenchikov, G., and Schulz, M.: The Geoengineering Model Intercomparison Project (GeoMIP), *Atmospheric Science Letters*, 12, 162–167, <https://doi.org/10.1002/asl.316>, 2011.
- 545 Kremser, S., Thomason, L. W., von Hobe, M., Hermann, M., Deshler, T., Timmreck, C., Toohey, M., Stenke, A., Schwarz, J. P., Weigel, R., Fueglistaler, S., Prata, F. J., Vernier, J.-P., Schlager, H., Barnes, J. E., Antuña-Marrero, J.-C., Fairlie, D., Palm, M., Mahieu, E., Notholt, J., Rex, M., Bingen, C., Vanhellefont, F., Bourassa, A., Plane, J. M. C., Klocke, D., Carn, S. A., Clarisse, L., Trickl, T., Neely, R., James, A. D., Rieger, L., Wilson, J. C., and Meland, B.: Stratospheric aerosol – Observations, processes, and impact on climate, *Rev. Geophys.*, 54, 278–335, <https://doi.org/https://doi.org/10.1002/2015RG000511>, 2016.
- 550 Kulmala, M. and Laaksonen, A.: Binary nucleation of water–sulfuric acid system: Comparison of classical theories with different H<sub>2</sub>SO<sub>4</sub> saturation vapor pressures, *J. Chem. Phys.*, 93, 696–701, <https://doi.org/10.1063/1.459519>, 1990.
- Laakso, A., Niemeier, U., Visionsi, D., Tilmes, S., and Kokkola, H.: Dependency of the impacts of geoengineering on the stratospheric sulfur injection strategy – Part 1: Intercomparison of modal and sectional aerosol modules, *Atmos. Chem. Phys.*, 22, 93–118, <https://doi.org/10.5194/acp-22-93-2022>, 2022.
- 555 Mauritsen, T., Bader, J., Becker, T., Behrens, J., Bittner, M., Brokopf, R., Brovkin, V., Claussen, M., Crueger, T., Esch, M., Fast, I., Fiedler, S., Fläschner, D., Gayler, V., Giorgetta, M., Goll, D. S., Haak, H., Hagemann, S., Hedemann, C., Hohenegger, C., Ilyina, T., Jahns, T., Jimenez-de-la Cuesta, D., Jungclaus, J., Kleinen, T., Kloster, S., Kracher, D., Kinne, S., Kleberg, D., Lasslop, G., Kornbluh, L., Marotzke, J., Matei, D., Meraner, K., Mikolajewicz, U., Modali, K., Möbis, B., Müller, W. A., Nabel, J. E. M. S., Nam, C. C. W., Notz, D., Nyawira, S.-S., Paulsen, H., Peters, K., Pincus, R., Pohlmann, H., Pongratz, J., Popp, M., Raddatz, T. J., Rast, S., Redler, R., Reick, C. H., Rohrschneider, T., Schemann, V., Schmidt, H., Schnur, R., Schulzweida, U., Six, K. D., Stein, L., Stemmler, I., Stevens, B., von
- 560





- Storch, J.-S., Tian, F., Voigt, A., Vrese, P., Wieners, K.-H., Wilkenskjeld, S., Winkler, A., and Roeckner, E.: Developments in the MPI-M Earth System Model version 1.2 (MPI-ESM1.2) and Its Response to Increasing CO<sub>2</sub>, *Journal of Advances in Modeling Earth Systems*, 11, 998–1038, <https://doi.org/https://doi.org/10.1029/2018MS001400>, 2019.
- 565 National Research Council: *Climate Intervention: Reflecting Sunlight to Cool Earth*, The National Academies Press, Washington, DC, <https://doi.org/10.17226/18988>, 2015.
- Niemeier, U. and Timmreck, C.: What is the limit of climate engineering by stratospheric injection of SO<sub>2</sub>?, *Atmos. Chem. Phys.*, 15, 9129–9141, <https://doi.org/10.5194/acp-15-9129-2015>, 2015.
- Niemeier, U., Schmidt, H., and Timmreck, C.: The dependency of geoengineered sulfate aerosol on the emission strategy, *Atmospheric Science Letters*, 12, 189–194, <https://doi.org/10.1002/asl.304>, 2011.
- 570 Pierce, J. R., Weisenstein, D. K., Heckendorn, P., Peter, T., and Keith, D. W.: Efficient formation of stratospheric aerosol for climate engineering by emission of condensable vapor from aircraft, *Geophys. Res. Lett.*, 37, <https://doi.org/10.1029/2010GL043975>, 2010.
- Quaglia, I., Timmreck, C., Niemeier, U., Visionsi, D., Pitari, G., Brodowsky, C., Brühl, C., Dhomse, S. S., Franke, H., Laakso, A., Mann, G. W., Rozanov, E., and Sukhodolov, T.: Interactive stratospheric aerosol models’ response to different amounts and altitudes of SO<sub>2</sub> injection during the 1991 Pinatubo eruption, *Atmospheric Chemistry and Physics*, 23, 921–948, <https://doi.org/10.5194/acp-23-921-2023>, 2023.
- 575 Roeckner, E., Bäuml, G., Bonaventura, L., Brokopf, R., Esch, M., Giorgetta, M., Hagemann, S., Kirchner, I., Kornblueh, L., Manzini, E., Rhodin, A., Schlese, U., Schulzweida, U., and Tompkins, A.: The atmospheric general circulation model ECHAM 5. PART I: Model description, MPI-Report No. 349, Max-Planck-Institut für Meteorologie, Hamburg, [http://www.mpimet.mpg.de/fileadmin/publikationen/Reports/max\\_scirep\\_349.pdf](http://www.mpimet.mpg.de/fileadmin/publikationen/Reports/max_scirep_349.pdf), 2003.
- 580 Roeckner, E., Brokopf, R., Esch, M., Giorgetta, M., Hagemann, S., Kornblueh, L., Manzini, E., Schlese, U., and Schulzweida, U.: Sensitivity of simulated climate to horizontal and vertical resolution in the ECHAM5 atmosphere model, *J. Climate*, 19, 3771–3791, <https://doi.org/10.1175/JCLI3824.1>, 2006.
- Rozanov, E. V., Zubov, V. A., Schlesinger, M. E., Yang, F., and Andronova, N. G.: The UIUC three-dimensional stratospheric chemical transport model: Description and evaluation of the simulated source gases and ozone, *J. Geophys. Res.*, 104, 11 755–11 781, <https://doi.org/10.1029/1999JD900138>, 1999.
- 585 Seinfeld, J. H. and Pandis, S. N.: *Atmospheric Chemistry and Physics: From Air Pollution to Climate Change*, John Wiley & Sons Inc., 1997.
- Sheng, J., Weisenstein, D. K., Luo, B., Rozanov, E., Stenke, A., Anet, J., Bingemer, H., and Peter, T.: Global atmospheric sulfur budget under volcanically quiescent conditions: Aerosol-chemistry-climate model predictions and validation, *J. Geophys. Res.- Atmos.*, 120, 256–276, <https://doi.org/10.1002/2014JD021985>, 2015.
- 590 Solomon, S.: Stratospheric ozone depletion: A review of concepts and history, *Rev. Geophys.*, 37, 275–316, <https://doi.org/doi:10.1029/1999RG900008>, 1999.
- Stenke, A., Schraner, M., Rozanov, E., Egorova, T., Luo, B., and Peter, T.: The SOCOL version 3.0 chemistry–climate model: description, evaluation, and implications from an advanced transport algorithm, *Geosci. Model Dev.*, 6, 1407–1427, <https://doi.org/10.5194/gmd-6-1407-2013>, 2013.
- 595 Stenke, A., Vattioni, S., Chiodo, G., Luo, B., Sukhodolov, T., and Peter, T.: Simulation data for testing the aerosol microphysical scheme of SOCOL-AERv2, ETH Zurich, <https://doi.org/10.3929/ethz-b-000610854>, 2023.



- Stier, P., Feichter, J., Kinne, S., Kloster, S., Vignati, E., Wilson, J., Ganzeveld, L., Tegen, I., Werner, M., Balkanski, Y., Schulz, M., Boucher, O., Minikin, A., and Petzold, A.: The aerosol-climate model ECHAM5-HAM, *Atmos. Chem. Phys.*, 5, 1125–1156,  
600 <https://doi.org/10.5194/acp-5-1125-2005>, 2005.
- Stott, P. A. and Harwood, R. S.: An implicit time-stepping scheme for chemical species in a global atmospheric circulation model, *Ann. Geophys.*, 11, 377–388, 1993.
- Sukhodolov, T., Sheng, J.-X., Feinberg, A., Luo, B.-P., Peter, T., Revell, L., Stenke, A., Weisenstein, D. K., and Rozanov, E.: Stratospheric aerosol evolution after Pinatubo simulated with a coupled size-resolved aerosol–chemistry–climate model, SOCOL-AERv1.0, *Geosci. Model Dev.*, 11, 2633–2647, <https://doi.org/10.5194/gmd-11-2633-2018>, 2018.  
605
- Sukhodolov, T., Egorova, T., Stenke, A., Ball, W. T., Brodowsky, C., Chiodo, G., Feinberg, A., Friedel, M., Karagodin-Doyennel, A., Peter, T., Sedlacek, J., Vattioni, S., and Rozanov, E.: Atmosphere–ocean–aerosol–chemistry–climate model SOCOLv4.0: description and evaluation, *Geosci. Model Dev.*, 14, 5525–5560, <https://doi.org/10.5194/gmd-14-5525-2021>, 2021.
- Sun, H., Eastham, S., and Keith, D.: Developing a Plume-in-Grid Model for Plume Evolution in the Stratosphere, *J. Adv. Model. Earth Syst.*, 14, e2021MS002816, <https://doi.org/10.1029/2021MS002816>, 2022.  
610
- Tabazadeh, A., Toon, O. B., Clegg, S. L., and Hamill, P.: A new parameterization of H<sub>2</sub>SO<sub>4</sub>/H<sub>2</sub>O aerosol composition: Atmospheric implications, *Geophys. Res. Lett.*, 24, 1931–1934, <https://doi.org/10.1029/97GL01879>, 1997.
- Taylor, K. E., Williamson, D., and Zwiers, F.: The sea surface temperature and sea ice concentration boundary conditions for AMIP II simulations, Program for Climate Model Diagnosis and Intercomparison, PCMDI report 60, Lawrence Livermore National Laboratory,  
615 <https://pcmdi.llnl.gov/report/pdf/60.pdf?id=32>, (last access: 3 January 2023), 2000.
- Thomason, L. and Peter, T.: SPARC Assessment of Stratospheric Aerosol Properties (ASAP), SPARC Report No. 4, WCRP-124, WMO/TD-No. 1295, Stratospheric Processes And their Role in Climate (SPARC), <http://www.sparc-climate.org/publications/sparc-reports/>, (last access: 18 January 2023), 2006.
- Thomason, L. W., Ernest, N., Millán, L., Rieger, L., Bourassa, A., Vernier, J.-P., Manney, G., Luo, B., Arfeuille, F., and Peter, T.: A global space-based stratospheric aerosol climatology: 1979–2016, *Earth Syst. Sci. Data*, 10, 469–492,  
620 <https://doi.org/10.5194/essd-10-469-2018>, 2018.
- Tilmes, S., Richter, J. H., Mills, M. J., Kravitz, B., MacMartin, D. G., Garcia, R. R., Kinnison, D. E., Lamarque, J.-F., Tribbia, J., and Vitt, F.: Effects of Different Stratospheric SO<sub>2</sub> Injection Altitudes on Stratospheric Chemistry and Dynamics, *J. Geophys. Res.*, 123, 4654–4673, <https://doi.org/10.1002/2017JD028146>, 2018.
- 625 Timmreck, C., Mann, G. W., Aquila, V., Hommel, R., Lee, L. A., Schmidt, A., Brühl, C., Carn, S., Chin, M., Dhomse, S. S., Diehl, T., English, J. M., Mills, M. J., Neely, R., Sheng, J., Toohey, M., and Weisenstein, D.: The Interactive Stratospheric Aerosol Model Intercomparison Project (ISA-MIP): motivation and experimental design, *Geosci. Model Dev.*, 11, 2581–2608, <https://doi.org/10.5194/gmd-11-2581-2018>, 2018.
- Vattioni, S., Weisenstein, D., Keith, D., Feinberg, A., Peter, T., and Stenke, A.: Exploring accumulation-mode H<sub>2</sub>SO<sub>4</sub> versus SO<sub>2</sub> stratospheric sulfate geoengineering in a sectional aerosol–chemistry–climate model, *Atmos. Chem. Phys.*, 19, 4877–4897,  
630 <https://doi.org/10.5194/acp-19-4877-2019>, 2019.
- Vattioni, S., Stenke, A., C.-G., Luo, B., Sukhodolov, T., and Peter, T.: Simulation data for testing the aerosol microphysical scheme of SOCOL-AERv2, ETH Zurich, <https://doi.org/10.3929/ethz-b-000622193>, 2023.



- 635 Vehkamäki, H., Kulmala, M., Napari, I., Lehtinen, K. E. J., Timmreck, C., Noppel, M., and Laaksonen, A.: An improved parameterization  
for sulfuric acid–water nucleation rates for tropospheric and stratospheric conditions, *J. Geophys. Res.*, 107, AAC 3–1–AAC 3–10,  
<https://doi.org/10.1029/2002JD002184>, 2002.
- Visioni, D., Jones, A., Haywood, J., Séférian, R., Nabat, P., Boucher, O., Bednarz, E. M., Niemeier, U., et al.: Stratospheric ozone response  
to sulfate aerosol and solar dimming climate interventions based on the G6 Geoengineering Model Intercomparison Project (GeoMIP)  
simulations, *Atmospheric Chemistry and Physics*, 22, 4557–4579, 2022.
- 640 Walcek, C. J.: Minor flux adjustment near mixing ratio extremes for simplified yet highly accurate monotonic calculation of tracer  
advection, *J. Geophys. Res.*, 105, 9335–9348, <https://doi.org/10.1029/1999JD901142>, 2000.
- Wan, H., Rasch, P. J., Zhang, K., Kazil, J., and Leung, L. R.: Numerical issues associated with compensating and competing processes in  
climate models: an example from ECHAM-HAM, *Geosci. Model Dev.*, 6, 861–874, <https://doi.org/10.5194/gmd-6-861-2013>, 2013.
- Weisenstein, D. K., Yue, G. K., Ko, M. K., Sze, N., Rodriguez, J. M., and Scott, C. J.: A two-dimensional model of sulfur species and  
645 aerosols, *J. Geophys. Res.*, 102, 13 019–13 035, <https://doi.org/10.1029/97JD00901>, 1997.
- Weisenstein, D. K., Penner, J. E., Herzog, M., and Liu, X.: Global 2-d intercomparison of sectional and modal aerosol modules, *Atmos.  
Chem. Phys.*, 7, 2339–2355, <https://doi.org/10.5194/acp-7-2339-2007>, 2007.
- Weisenstein, D. K., Visioni, D., Franke, H., Niemeier, U., Vattioni, S., Chiodo, G., Peter, T., and Keith, D. W.: An interactive stratospheric  
aerosol model intercomparison of solar geoengineering by stratospheric injection of SO<sub>2</sub> or accumulation-mode sulfuric acid aerosols,  
650 *Atmos. Chem. Phys.*, 22, 2955–2973, <https://doi.org/10.5194/acp-22-2955-2022>, 2022.
- Yu, F., Nadykto, A. B., Luo, G., and Herb, J.: H<sub>2</sub>SO<sub>4</sub>–H<sub>2</sub>O binary and H<sub>2</sub>SO<sub>4</sub>–H<sub>2</sub>O–NH<sub>3</sub> ternary homogeneous and ion-mediated  
nucleation: lookup tables version 1.0 for 3-D modeling application, *Geosci. Model Dev.*, 13, 2663–2670,  
<https://doi.org/10.5194/gmd-13-2663-2020>, 2020.
- Yu, F., Luo, G., Nair, A. A., Eastham, S., Williamson, C. J., Kupc, A., and Brock, C. A.: Particle number concentrations and size  
655 distributions in the stratosphere: implications of nucleation mechanisms and particle microphysics, *Atmos. Chem. Phys.*, 23, 1863–1877,  
<https://doi.org/10.5194/acp-23-1863-2023>, 2023.